Article

Dynamic Analysis of Shared Moorings in Different Wind Farm Layouts

Marcus Vinícius Biroli, Felipe José Vidal, Juliana Desiderati, Shan Wang * and C. Guedes Soares

Centre for Marine Technology and Ocean Engineering (CENTEC), Instituto Superior Técnico, Universidade de Lisboa, 1049-001 Lisboa, Portugal; marcusbiroli@tecnico.ulisboa.pt (M.V.B.); felipe.vidal@tecnico.ulisboa.pt (F.J.V.); juliana.desiderati@tecnico.ulisboa.pt (J.D.); c.guedes.soares@centec.tecnico.ulisboa.pt (C.G.S.)

* Corresponding author. E-mail: shan.wang@centec.tecnico.ulisboa.pt (S.W.)

ABSTRACT: The effects of shared mooring in offshore wind farms are investigated through numerical simulations in the present study. Different farm layouts are modelled and tested in SIMA coupled dynamic analysis software with three and four floaters. The wind turbine and the platform are based on the OC3 project from NREL: a 5-MW wind turbine and a spar floater with a 120-m draft. The water depth is 320 m, and the environmental loads are defined for an average operational condition. Firstly, the static results of the mooring line tension at the fairleads and anchors from the numerical model are compared with the values from the open-source MoorPy code. Then, domain simulations are conducted for three hours, and the dynamic behaviour of the floaters is analysed with a focus on surge and pitch motions. In addition, the dynamic stiffness effects of the polyester in the shared mooring line are considered in the SIMA simulations. The mooring line tensions are analysed, determining the global maximum tension across all systems. Results show that designs with two windward legs have significantly lower anchor mooring line tensions than those with a single windward leg, with no relevant variation in platform surge and pitch. Thus, the former systems are preferable for further investigation.

Keywords: Spar platform; Shared mooring; Offshore energy; Wind farm; Mooring dynamics

1. Introduction

With the growth of renewable energy, wind power plays an important role in the global energy transition. The demand for wind energy has increased to mitigate global warming caused by CO_2 emissions from fossil fuels [1]. This motivation became even more evident after implementing the Kyoto Protocol, which introduced limits on greenhouse gas emissions. Wind energy plays an essential role in helping countries meet the requirements of this protocol, which is reflected in the number of wind farms in operation and planning [2]. Anaya-Lara et al. [3] detailed that the energy from offshore wind turbines could replace fossil fuel-based power generation, reducing CO_2 emissions by approximately 300 g per kilowatt-hour when substituting natural gas, and about 700 g per kilowatt-hour when replacing coal-fired power plants. However, it is essential to mention that emission savings depend on how the wind farm is integrated into the overall power system.

The main advantage of offshore wind over onshore wind is the availability of greater wind resources. In offshore environments, wind speeds are higher and more uniform, improving power output. Due to the lower surface roughness, the turbulence is further reduced, resulting in a steady energy source for the grid [1,4]. In addition, because the air near the sea surface is less turbulent than on land, and the only design limitation is that the blades must remain above the maximum wave height expected in the sea state, offshore wind turbines can be placed lower, improving efficiency and stability. However, more challenges are involved in offshore floating wind turbines, such as the high costs [5], difficulties in installation and maintenance [6], and the harsh marine environment [7]. Despite these challenges, the market for this type of energy still looks promising [8].

The mooring system plays a crucial role in ensuring the reliability and safety of the floating system. The high Levelized Cost of Energy (LCOE) for floating offshore wind is currently three times that of fixed-bottom offshore wind,

posing a significant barrier to commercial deployment. Since mooring systems, including installation, account for approximately 20% of the capital expenditure (CAPEX) [9], optimising their design and deployment is crucial in lowering overall project costs and enhancing the commercial viability of floating wind farms.

The dynamic analysis of FOWTs involves evaluating the coupled behaviour of aerodynamic, hydrodynamic, structural, and control system dynamics. A common approach is aero-hydro-servo-elastic simulations, integrating wind turbine aerodynamics with platform hydrodynamics, mooring system dynamics, and control algorithms. Chen et al. [10] developed DARwind (Dynamic Analysis for Response of Wind Turbines), employing Kane's dynamical method and Cardan angles for kinematics while using the Blade Element Momentum (BEM) method for aerodynamics. Hydrodynamics were modelled through linear potential-flow theory, the Morison equation with strip theory, and additional damping corrections, while the mooring system followed a quasi-static procedure. Ramos-García et al. [11] implemented a hybrid lifting-line aerodynamic model with MIRAS and HAWC2, incorporating a filament-particle-mesh wake simulation. Their study demonstrated improved accuracy over traditional BEM but relied on Morison's equation and Airy wave theory for hydrodynamic interactions, though potential-flow theory outputs were also considered.

One important method for FOWT analysis is the low-fidelity frequency-domain modelling, which linearises system dynamics to assess natural frequencies, damping, and resonance effects. Dou et al. [12] used the QuLAF frequency-domain model to optimise floater responses under wind and wave loads. While the frequency-domain approach remains relevant for optimisation due to its better computational efficiency, the mid-fidelity time-domain method captures system nonlinearities, such as geometric and material effects. It enables both decoupled and coupled dynamic analyses [13]. Ma et al. [13] identified the coupled dynamic analysis as the offshore industry standard, as it improves upon decoupled methods by simultaneously computing the responses of all system components: mooring lines and floating platforms. High-fidelity Computational Fluid Dynamics (CFD) approaches, such as OpenFOAM, simulate air-ocean interactions using the Finite Volume Method (FVM) and Volume of Fluid (VOF) techniques [14].

To model rigid and flexible offshore body interactions, time-domain coupled dynamic analysis mid-fidelity software, such as SIMA (v4.8-01), OpenFAST (v8.16), OrcaFlex (v11.5e), and SIMPACK (v2024), may be used [15]. Thomsen et al. [16] used OpenFAST and OrcaFlex to simulate a TetraSpar FOWT, showing good agreement despite slight variations in pitch motion and natural periods due to differences in structural flexibility modelling. Chen and Hall [17] studied the coupling between the lumped-mass model code MoorDyn and the open-source CFD code OpenFOAM, showing that the results obtained from their coupled model had good agreement with experimental data. A benchmark study comparing many of the available codes was reported by Robertson et al. [18], which identifies the variety of formulations used and was used to quantify the uncertainty in those predictions [19].

In addition to numerical analysis, there have been many experimental investigations. Duan et al. [20] conducted an experimental investigation into the dynamic response of a single spar system. This study used a 1:50 scale model of the OC3 spar design, adapted for a water depth of 200 m. The results showed a significant influence of rotor rotation on yaw oscillation response. Furthermore, the tower-top bending moment oscillates primarily by a resonant response under wind-only excitation. They also found that the axial rotor thrust and the tower-top shear force exhibit similar behaviour. In wind-only conditions, both oscillate at the rotor's rotational frequency, the tower's first-mode natural frequency, and three times the rotor's speed, with the tower's first mode being dominant. However, when wind and waves act together, incident waves mainly drive their responses. Ahn and Shin [21] conducted experimental tests on a three-leg catenary spread mooring system in catenary configuration, showing a significant agreement between the experimental results and numerical simulations, such as those performed using OpenFAST. Similarly, Xu and Day [22] experimented on a spar platform under different environmental loads. Their study revealed a non-linear snatching behaviour in the mooring lines during regular wave tests, possibly leading to cable failure due to increased tension.

For many offshore floating platforms and other energy devices, due to large movements under extreme waves, snap loads appear on the mooring ropes, which damage the moorings and even reduce the entire system's life [23]. Examples of mooring line failure due to snap loads can be found in Kvitrud [24]. Therefore, for floating renewable energy systems, studying the ultimate load of mooring lines under survival conditions is of great significance to the development of the systems. Synthetic fibre ropes in hybrid moorings provide substantial economic and operational advantages, making them the preferred alternative to traditional chains in offshore renewable energy (ORE) mooring configurations [25–28], however the typical fibre ropes in marine applications, such as polyester, HMPE and nylon ropes exhibit complex non-linear mechanical behaviours [29–31]. Proper consideration of mooring rope material nonlinearity can lead to more accurate predictions when exploring the coupled hydrodynamic performance of FOWTs [32] and shallow water ORE devices [33].

On the other hand, to reduce the costs of anchors and moorings in Floating Offshore Wind Farms (FOWFs), shared mooring and anchor system have gained increasing interest in academia and industry in recent years. Liang et al. [34] propose a two-turbine layout. The design is based on the OC3 Hywind project from the National Renewable Energy Laboratory (NREL). The spacing between turbines is set at 1000 m, and the anchor radius is increased by 100 m compared to the original single-spar model. The angle between the anchor lines from the same spar is set at 120°. The study compares the dynamic results with the single-turbine system under extreme environmental conditions. Goldschmidt and Muskulus [35] investigate row, triangular, and rectangular layouts of FOWTs to reduce project costs. The study employs coupled catenary mooring and analyses the dynamic behaviour in the frequency domain. A 60% reduction in mooring costs and an 8% reduction in the total system cost were estimated in the rectangular configuration. Goldschmidt and Muskulus [35] concluded that the row layout is optimal for a three-spar system. The dynamic behaviour of Floating Offshore Wind Turbines (FOWTs) with shared mooring was also investigated by Lopez-Olocco et al. [36]. Experimental simulations were conducted using a 1:47 scale spar model with catenary mooring under operational and extreme sea conditions. The results for a dual-spar system with a shared line were compared to those of a single-spar system. One important finding was that the surge natural period is about 51% longer for the dual system than for the single one, likely due to differences in mooring stiffness and restoring forces. In addition, they observed through spectral analysis that the tension in the shared line presents a dominant peak response in the first-order wave frequency range. Hall et al. [37] also investigated shared mooring lines. Their study modelled a system with ten FOWTs using MoorPy, an open-source code for quasi-static analysis. The results show that combining shared lines with shared anchors may significantly reduce installation costs. The present study investigates platform motions and mooring line tensions under different shared mooring layouts. The quasi-static analysis for several layouts is performed using the open-source code MoorPy. The fully coupled dynamic analysis is conducted using SIMA while considering the dynamic stiffness of synthetic ropes, modelling using the Syrope model from DNV [38]. The motions of the floaters and the mooring tensions at the fairleads and anchor points are compared and discussed.

2. Methodology

The present study performs a fully coupled dynamic analysis using the commercial software SIMA (v4.8-01), part of the DNV SESAM package [39]. It enables coupled analysis by integrating RIFLEX for line dynamics and SIMO for body dynamics, offering a comprehensive simulation framework.

2.1. Body Forces

The forces are modelled in SIMO to represent the interactions between the body and the environment accurately. These models incorporate various forces, including hydrodynamic, hydrostatic, and aerodynamic forces, as well as forces from mooring systems or other station-keeping mechanisms. The general equation of motion for a system experiencing sinusoidal motion is expressed as in Equation (1).

$$M\ddot{x} + C\dot{x} + D_1\dot{x} + D_2 f(\dot{x}) + K(x)x = q(t, x, \dot{x}) \tag{1}$$

where: M is the frequency-dependent mass matrix, which can be rewritten with the body mass matrix and added mass, as $(m + A(\omega))$; C is the frequency-dependent potential damping matrix; D_1 is the linear damping matrix; D_2 is the quadratic damping matrix; K is the hydrostatic stiffness.

Excitation forces are the summation of external forces, including wind drag, first- and second-order wave excitation, current drag, wave drift damping, and other external forces. These forces are represented in the relation present in Equation (2).

$$q(t, x, \dot{x}) = q_{WI} + q_{WA}^{(1)} + q_{WA}^{(2)} + q_{CU} + q_{ext} \tag{2}$$

2.2. Mooring Calculation

Initially, the RIFLEX module solves the catenary equation by considering any number of segments of different materials, the rigid-body equilibrium of articulated elements, clump weights and buoys, and seabed contact [39]. Then, the mooring lines are discretised in bar elements, and a finite element analysis (FEA) is conducted to find static and dynamic solutions. The FEA procedure considers the damping, current drag, and additional mass, which are calculated using Morison's equation and the axial stiffness of the element. Notably, the particularities of the synthetic material must be well modelled for polyester mooring lines due to their importance in the proposed farm designs.

The shared lines, key to system response, particularly the surge, are entirely made of polyester, eliminating the need for a clumped weight required in chain legs, which is cost-effective. However, synthetic fibre ropes have non-linear load-elongation curves, exhibit plastic deformation, and present significantly higher stiffness in dynamic conditions. Vidal et al. [40] state the Syrope as the most accurate polyester stiffness model, covering the identified traits, and it is implemented following their procedure.

2.3. Wave Load

In addition to the body forces, SIMO is also responsible for generating time series and modelling the equations of motion for environmental loads. According to the SIMA manual [39], the irregular wave model may consider the summation of two spectra: the wind sea and swell contributions [41]. This study considers an irregular wind wave modelled as a three-parameter JONSWAP spectrum, which is defined as:

$$S(\omega) = \frac{\alpha g^2}{\omega^5} \exp\left[-1.25 \left(\frac{\omega_p}{\omega}\right)^4\right] \gamma^{\exp\left[-\frac{\left(\frac{\omega}{\omega_p}-1\right)^2}{2\sigma^2}\right]} \tag{3}$$

where: γ is the peakedness parameter; σ and α are the spectral parameters, defined as a function of the significant wave height H_s and peak period T_p:

$$\sigma = \begin{cases} 0.07 & \omega \leq \omega_p \\ 0.09 & \omega > \omega_p \end{cases} \tag{4}$$

$$\alpha = 5.061 \frac{H_s^2}{T_p^4} (1 - 0.287 \ln(\gamma)) \tag{5}$$

3. Description of the FOWFs

3.1. Platform and Wind Turbine

Both the platform and wind turbine are from the OC3 project [42] as a design basis. The spar floater is commonly used in deepwater projects due to its low centre of mass, enhancing the overall platform stability. The reduced waterline area makes the platform less responsive to the waves. The main properties of the platform can be found in Table 1. The NREL wind turbine [43] has a power capacity of 5 MW, and it is placed 10 m above the still waterline. The specifications of the structure are detailed in Table 2.

Table 1. Properties of the OC3 spar platform.

Parameter	Value	Unit
Depth to platform base below SWL	120.00	m
Water displaced volume	8029.20	m^3
Depth to top and bottom of taper below SWL	4.00, 12.00	m
Platform diameter above and below taper	6.50, 9.40	m
Platform mass, including ballast	7466.33	tonnes
Centre of mass height	−89.92	m

Table 2. Properties of the 5-MW wind turbine.

Parameter	Value	Unit
Hub height	90.00	m
Hub diameter	3.00	m
Blade length	61.50	m
Tower mass	249.72	tonnes
Blade mass	17.74	tonnes

3.2. System Layouts

The three-spar system layouts were based on the study by Fu et al. [44], which examines the aerodynamic performance and wake characteristics of three fixed wind turbines using Large Eddy Simulation (LES) and the Actuator Line Model (ALM). Their research aimed to understand how the varying interactions of wake influence the efficiency of power generation and the overall aerodynamic performance of wind farms.

Fu et al. [44] found the most efficient set-up was the tandem arrangement, where the three turbines were aligned. In a full wind wake condition, the distance between the turbines has little effect on the power and thrust of the middle turbine, but it significantly impacts the downstream turbine. Moreover, when the distance between the first and middle turbines is reduced, the total power of the three-turbine system tends to increase. The system was modelled with 4 and 6 anchors (Figure 1), with an angle of 120° between anchor lines, to assess the effect of the middle lines on the restoring forces.
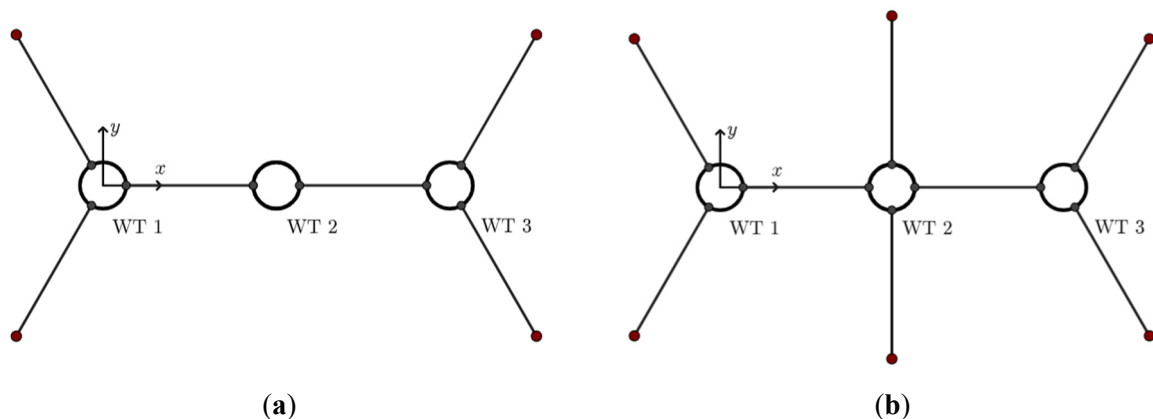

Figure 1. A three-spar system is in tandem arrangement, with (**a**) four anchors and (**b**) six anchors.

In a staggered setup of three turbines, two configurations are proposed: with two downstream wind turbines or with two upstream. In the first case, the turbulence affects the downstream turbines from one side, causing notable changes in thrust and torque. However, when the turbulence comes from both sides, the thrust and torque are more stable in the case of two upstream turbines. The two turbines in front speed up the wind for the downstream turbine, leading to a noticeable increase in its power output.

Since the platforms were studied as fixed turbines, it is important to perform simulations for all configurations to obtain the tensions from the floating systems and analyse the pitch motion, which directly affects the farm's energy production [45]. Both staggered systems are modelled triangularly, where the anchor line is aligned with the triangle's median. The layouts are displayed in Figure 2.
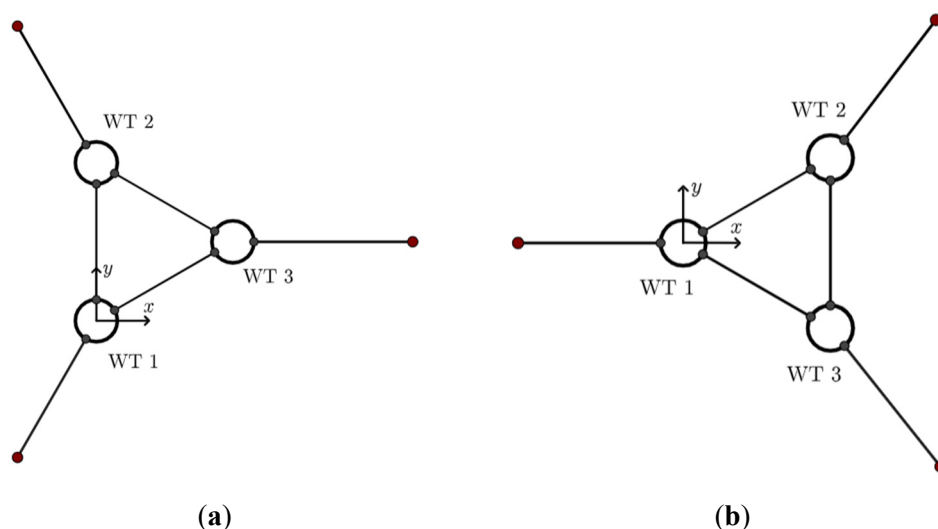

Figure 2. A three-spar system is in a staggered arrangement, with (**a**) two upstream wind turbines and (**b**) two downstream wind turbines.

In addition to the three-spar system, two new concepts of four-spar systems are proposed (Figure 3). The first one consists of perpendicular shared lines, where each turbine has two shared moorings and one anchor. The anchor moorings present an angle of 45° in relation to the axes. The second system presents shared lines at an angle of 30 degrees in relation to the *x*-axis. This concept guarantees that turbines 2 and 3 have the same distance between them and between the other two turbines.
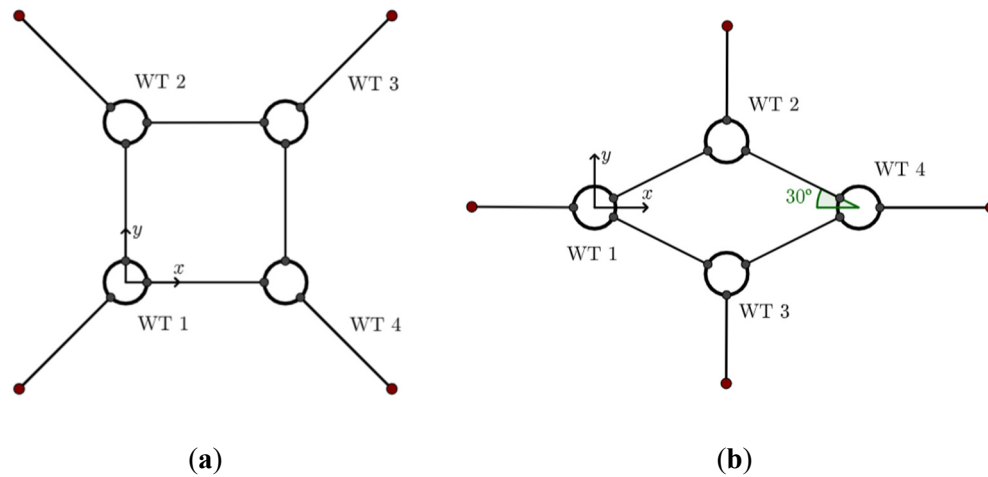

(a)	(b)

Figure 3. A four-spar system, with an angle between the shared line and *x*-axis of: (**a**) 90 degrees; (**b**) 30 degrees.

3.3. Mooring Properties

The mooring properties for the anchored lines are taken from Jonkman [42]. This material, used in the OC3 project, is a multisegmented mooring with the properties shown in Table 3, simplified by the weighted-average values of the parameters displayed. The shared lines between platforms are composed entirely of polyester, with properties from the Bridon Fiber Rope catalogue [46]. The polyester length equals the initial spacing between floaters, which is defined as five times the rotor diameter, or 630 m. The diameter originates from the results of Biroli et al. [47], where a numerical study of a dual-spar system was performed, and the polyester with a 139 mm diameter showed stable results with low tensions at the fairleads. The anchor radius is set at a horizontal distance of 853.87 m from the platform's centreline.

Table 3. Mooring main parameters.

Parameter	OC3 Mooring	Polyester	Unit
Diameter	90.00	139.00	mm
Length	902.20	630.00	m
Mass density	77.71	12.10	kg/m
Weight in water	698.09	29.43	N/m
Extensional stiffness	3.84×10^8	*	N
Maximum breaking load	- **	4.91×10^6	N

* Syrope model, please refer to Section 2.2. ** No data available.

3.4. Environmental Parameters

The irregular waves are modelled using a JONSWAP three-parameter model. The significant wave height (Hs) and peak period are defined based on average sea states observed in experimental studies [20,21]. Wind speed is set at the rated speed of 11.4 m/s and modelled as a stationary uniform flow. The peak-spectra parameter (γ) is obtained from the design load condition defined by Balakrishnan et al. [48]. A regular sea current of 1 m/s is implemented. All environmental loads are unidirectional; therefore, the dynamic forces are applied only along the *x*-axis. The parameters are shown in Table 4.

Table 4. Environmental parameters.

Hs	Tp	γ	Wind Speed	Current Speed
m	S	- *	m/s	m/s
5.49	11.30	2.00	11.40	1.00

* No unit.

4. Results and Discussion

4.1. Static Results

The static results are obtained with the SIMA (v4.8-01) software without considering any environmental loads and are then verified with MoorPy, an open-source code for quasi-static analysis [49]. This code does not support the Syrope model. Thus, following Vidal et al.'s [40] approach, a representative constant axial stiffness (from the load-elongation curve) was identified and used for each quasi-static comparison. The points studied in this test are the anchored line fairlead (Fairlead AL), the shared line fairlead (Fairlead SL), and the anchor. The motion results are related to the platform's initial position.

Firstly, both tandem systems were evaluated. The defined axial stiffness for the system with four and six anchors was 26.8 MN and 28.0 MN, respectively. The tension values in each point are detailed in Table 5. In addition, for these systems, the initial displacements in the *x* and *z* directions are obtained and presented in Table 6. The Moorpy static plots are shown in Figure 4.

Table 5. Static tensions for three-spar systems in tandem arrangement.

Turbine	Point	Tandem Four Anchors			Tandem Six Anchors		
		SIMA [kN]	MoorPy [kN]	Difference [kN]	SIMA [kN]	MoorPy [kN]	Difference [kN]
WT1 & WT3	Fairlead AL	772.66	774.20	1.54	776.97	778.62	1.65
	Fairlead SL	584.44	584.20	0.24	589.19	589.08	0.12
	Anchor	599.18	598.58	0.60	603.49	603.02	0.47
WT2	Fairlead AL	- *	- *	- *	925.35	926.32	0.97
	Fairlead SL	584.52	584.28	0.24	589.18	589.07	0.11
	Anchor	- *	- *	- *	752.00	751.00	1.00

* No anchor lines attached to WT2 for tandem configuration with four anchors.

Table 6. Static initial displacement for three-spar systems in tandem arrangement.

Initial Displacement	Turbine	Tandem Four Anchors			Tandem Six Anchors		
		SIMA [m]	MoorPy [m]	Difference [m]	SIMA [m]	MoorPy [m]	Difference [m]
X	WT1	−13.72	−13.56	0.15	−13.26	−13.10	0.16
	WT2	−0.09	0.00	0.09	−0.08	0.00	0.08
	WT3	13.60	13.56	0.04	13.10	13.10	0.00
Z	WT1	2.03	1.94	0.09	2.01	1.92	0.09
	WT2	4.92	4.83	0.09	1.69	1.60	0.09
	WT3	2.03	1.94	0.09	2.01	1.92	0.09

Due to the system's symmetry, wind turbines 1 and 3 (upstream and downstream) have the same values for tension and displacement. The SIMA results show a small difference in the surge motion values. This discordance is likely due to the platform definition of centre of mass on the SIMA model, where the wind turbine hub and blades shift the centre of mass away from the centreline, causing mass asymmetry on the system. The polyester shared line presents a different tension at each end since the platforms connected have a different displacement in the *z*-axis.

The staggered configurations have the same mooring design. The main difference between the systems' models is the coordinate system and turbine orientation. Therefore, for both systems, the axial stiffness is defined as 26.3 MN, and the tensions are displayed together in Table 7. For convenience, the translational motions are shown in Table 8 only for the system with two upstream wind turbines. The system representation is shown in Figure 5.
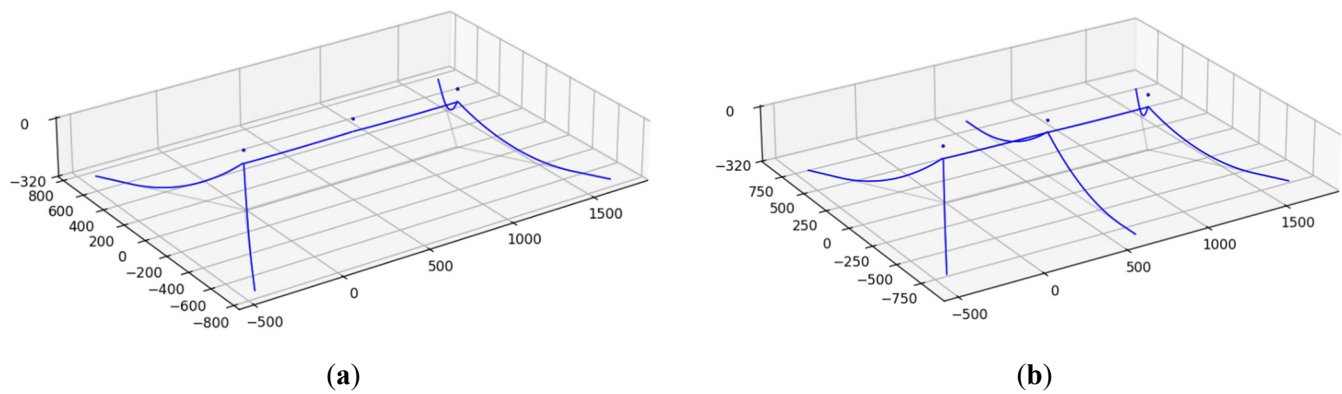
Figure 4. MoorPy static plot for three-spar system in tandem arrangement, with: (**a**) four anchors; (**b**) six anchors.

Table 7. Static tensions for three-spar systems in staggered arrangement.

Turbine	Point	SIMA [kN]	MoorPy [kN]	Difference [kN]
WT1, WT2 & WT3	Fairlead AL	815.98	820.50	4.52
	Fairlead SL	370.44	368.78	1.66
	Anchor	641.51	643.94	2.43

Table 8. Static initial displacement for three-spar system in staggered arrangement with two upstream wind turbines.

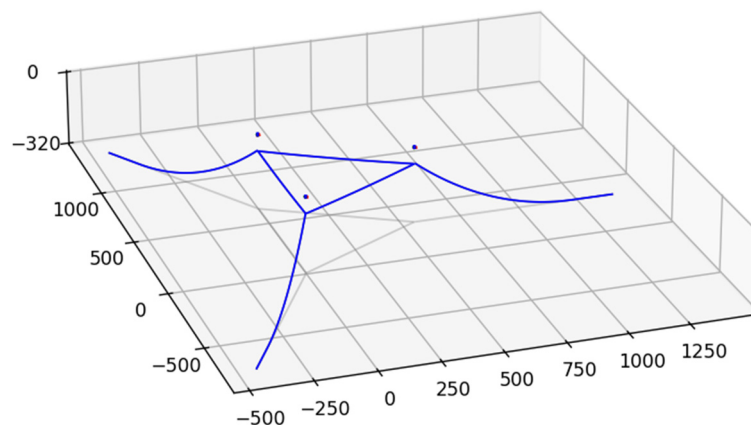| Initial Displacement	Turbine	SIMA [m]	MoorPy [m]	Difference [m]
X	WT1	−2.72	−2.53	0.19
	WT2	−2.72	−2.53	0.19
	WT3	5.18	5.07	0.12
Y	WT1	−4.57	−4.39	0.18
	WT2	4.57	4.39	0.18
	WT3	0.00	0.00	0.00
Z	WT1	3.42	3.33	0.09
	WT2	3.42	3.33	0.09
	WT3	3.42	3.33	0.09

Figure 5. MoorPy static plot for a three-spar system in staggered arrangement.

In static equilibrium, the three turbines have the same values for tension since the system is symmetric and exhibits the same vertical displacement. The tension at the anchor line fairlead presents values twice as large as those of the shared line. It was found that, for the four-spar systems, the constant axial stiffness of 33.0 MN and 34.8 MN were good representations for the configurations with 90- and 30-degree orientations, respectively. The tensions are displayed in Table 9, and the platform displacement in all directions is detailed in Table 10. The MoorPy models are shown in Figure 6.

The tension results for the four-spar system with shared moorings at 90 degrees are the same for all floaters, since the system is symmetric in every direction. However, the system at 30 degrees exhibits symmetry between wind turbines

1 & 4 and turbines 2 & 3. Because of this, the tensions are better distributed in the first system (Figure 6a) than in the second (Figure 6b), where the maximum static tension is 17.41% higher.

Table 9. Static tensions for four-spar systems.

Turbine	Point	Four-Spar 90 Degrees			Four-Spar 30 Degrees		
		SIMA [kN]	MoorPy [kN]	Difference [kN]	SIMA [kN]	MoorPy [kN]	Difference [kN]
WT1 & WT4	Fairlead AL	798.10	803.34	5.24	937.04	939.06	2.02
	Fairlead SL	440.97	438.13	2.84	445.87	445.92	0.05
	Anchor	623.62	626.76	3.14	762.58	762.63	0.05
WT2 & WT3	Fairlead AL	798.10	803.34	5.24	636.69	638.83	2.14
	Fairlead SL	440.97	438.13	2.84	445.88	445.91	0.03
	Anchor	623.62	626.76	3.14	462.24	462.05	0.19

Table 10. Static initial displacement for four-spar systems.

| Initial Displacement	Turbine	Four-Spar 90 Degrees			Four-Spar 30 Degrees		
		SIMA [m]	MoorPy [m]	Difference [m]	SIMA [m]	MoorPy [m]	Difference [m]
X	WT1	−4.41	−4.15	0.25	−0.37	−0.19	0.18
	WT2	−4.41	−4.15	0.25	−0.09	0.00	0.09
	WT3	4.24	4.15	0.09	−0.09	0.00	0.09
	WT4	4.24	4.15	0.09	0.21	0.19	0.02
Y	WT1	−4.32	−4.15	0.17	0.00	0.00	0.00
	WT2	4.32	4.15	0.17	15.51	15.43	0.08
	WT3	−4.32	−4.15	0.17	−15.51	−15.43	0.08
	WT4	4.32	4.15	0.17	0.00	0.00	0.00
Z	WT1	3.43	3.34	0.09	3.30	3.20	0.09
	WT2	3.43	3.34	0.09	3.61	3.52	0.09
	WT3	3.43	3.34	0.09	3.61	3.52	0.09
	WT4	3.43	3.34	0.09	3.30	3.20	0.09

(a)   **(b)**
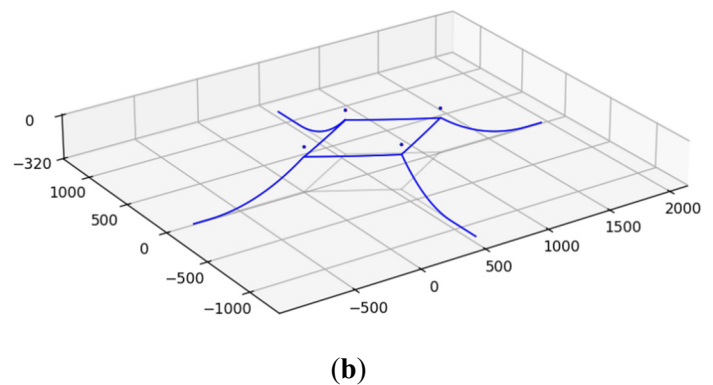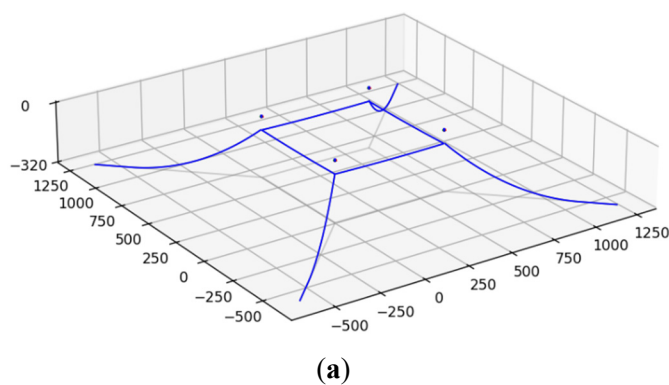
Figure 6. MoorPy static plot for four-spar system, with an angle between shared line and *x*-axis: (**a**) 90 degrees; (**b**) 30 degrees.

4.2. Dynamic Results

The fully coupled dynamic simulations are conducted for 3 h; however, the results are analysed from 7200 to 10,800 s. The tensions at symmetric x-axis points are practically the same; thus, the values presented in this section are the largest mean value. The tensions are analysed at the fairleads and anchors for all systems. In addition, the system's maximum global tension is defined to study the system's critical points. The six degrees of freedom (DOF) results obtained from SIMA, surge, and pitch motions are discussed in this section, since they are the most important DOF when analysing environmental loads applied along the *x*-axis.

The first system tested is the tandem arrangement with four anchors. The motion results are presented in Table 11, with the mean, maximum, minimum, and standard deviation values. A sample of their behaviour is displayed in Figure 7. The surge motion is shown in relation to the initial position. Wind turbine 1 presents the smallest offset from the initial position compared to the other two turbines. This is due to the two anchored lines that apply a restoring force over the two upstream fairleads. This is also noticeable in the pitch motion, where the upstream turbine presents a lower inclination.

Table 11. Surge and pitch motions for three-spar system in tandem arrangement with four anchors.

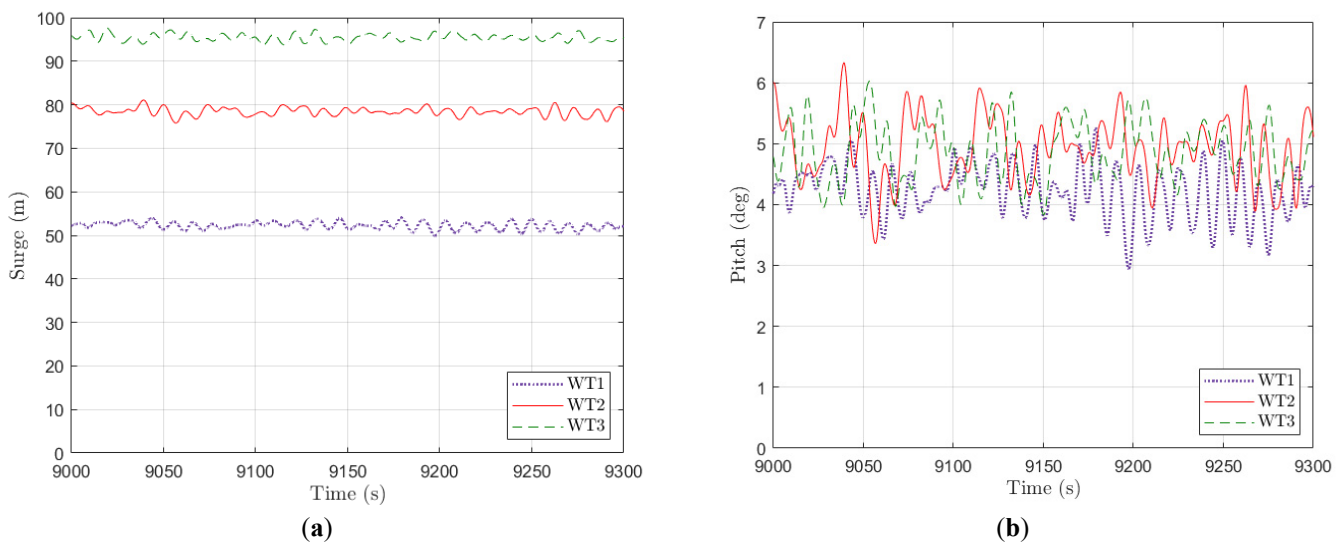| Motion	Turbine	Mean	Max	Min	Std
	WT1	52.42	55.06	49.91	0.781
Surge [m]	WT2	78.50	81.12	75.59	0.822
	WT3	95.53	97.60	92.70	0.819
	WT1	4.32	5.40	2.94	0.392
Pitch [deg]	WT2	4.94	6.33	3.36	0.440
	WT3	4.90	6.10	3.37	0.451

(a) (b)

Figure 7. Three-spar system in tandem arrangement with 4 anchors: (**a**) Surge motion; (**b**) Pitch motion.

The tensions for this simulation are presented in Table 12. In addition, a maximum tension distribution along the system is shown in Figure 8. The higher tensions are concentrated on the upstream area, where the upstream fairleads have the highest values in the entire system. In this model, there are no restoring forces on the middle turbine (WT2), therefore, the tension at the shared mooring between WT1 and WT2 reaches about 50% of the polyester's maximum breaking strength.

Table 12. Dynamic tension for a three-spar system in tandem arrangement with four anchors.

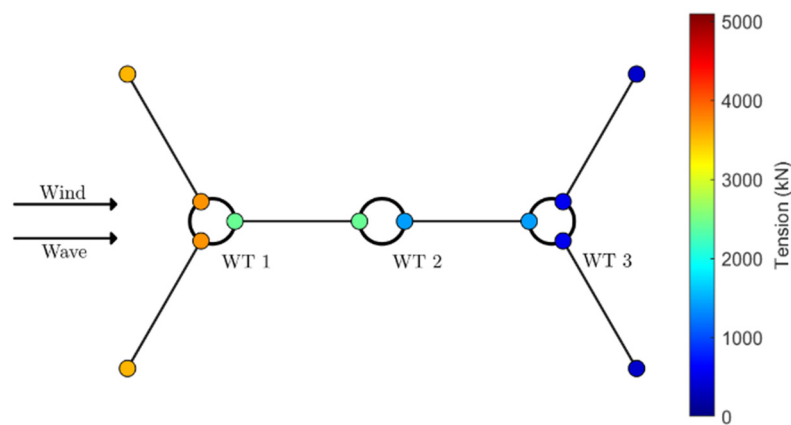| Location	Point	Mean [kN]	Max [kN]	Min [kN]	Std [kN]
	Upstream (WT1)	3132.40	3715.10	2559.00	165.02
Fairlead	Shared WT1-WT2	2143.90	2429.80	1840.70	91.16
	Shared WT2-WT3	1167.50	1416.90	906.89	81.61
	Downstream (WT3)	401.43	535.78	296.07	24.24
Anchor	Upstream (WT1)	2962.30	3547.60	2382.40	165.74
	Downstream (WT3)	228.03	365.20	94.07	30.55

Figure 8. Maximum tension distribution for a three-spar system in tandem arrangement with four anchors.

The second model tested is the tandem configuration with six anchors. This system adds two new anchor lines to the middle wind turbine. The motion results are detailed in Table 13, and their response is displayed in Figure 9. Compared to the 4 anchors layout, this system shows a lower mean displacement in surge due to the restoring forces now applied by the middle anchor lines. Because of this addition to the system, the value of the pitch motion of wind turbine 2 decreases, showing a more stable system. The obtained tensions, in both the fairlead and the anchor, are shown in Table 14. The tension distribution is displayed in Figure 10. The tensions are better distributed with the additional moorings. Therefore, the mean tension at the upstream fairleads and on the shared lines decreases.

Table 13. Surge and pitch motions for the three-spar system in tandem arrangement with six anchors.

Motion	Turbine	Mean	Max	Min	Std
Surge [m]	WT1	51.56	54.16	48.86	0.789
	WT2	75.69	78.18	72.70	0.823
	WT3	92.68	94.90	89.80	0.826
Pitch [deg]	WT1	4.32	5.45	2.84	0.396
	WT2	4.67	5.97	3.14	0.428
	WT3	4.89	6.14	3.47	0.453
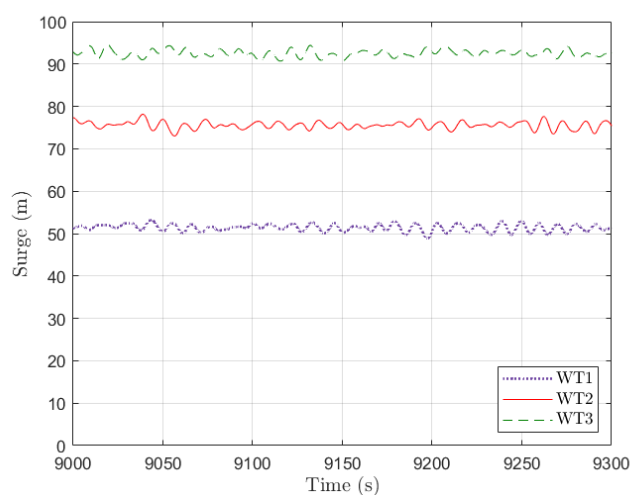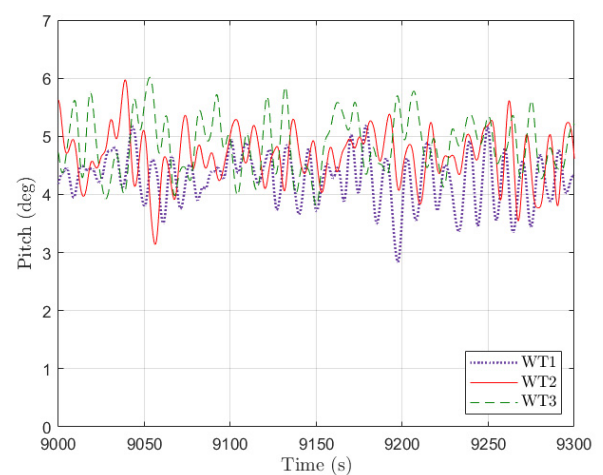
Figure 9. Three-spar system in tandem arrangement with six anchors: (**a**) Surge motion; (**b**) Pitch motion.
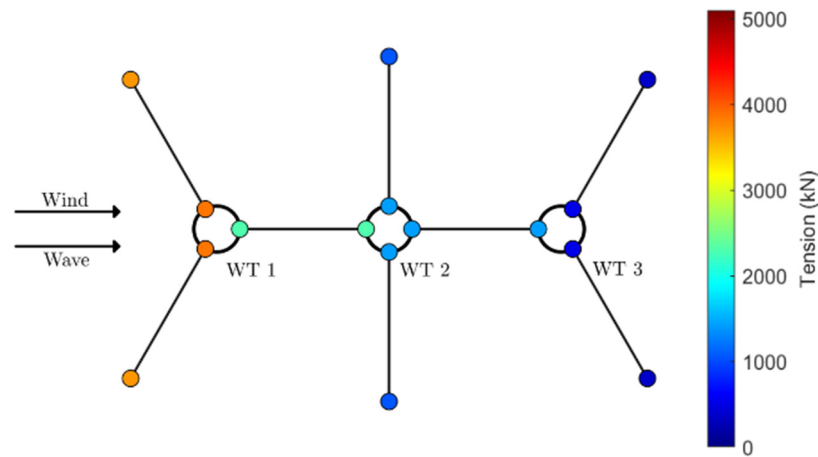
Figure 10. Maximum tension distribution for a three-spar system in tandem arrangement with six anchors.

Table 14. Dynamic tension for a three-spar system in tandem arrangement with six anchors.

Location	Point	Mean [kN]	Max [kN]	Min [kN]	Std [kN]
Fairlead	Upstream (WT1)	3018.10	3863.70	2335.80	246.67
	Shared WT1-WT2	2023.00	2305.20	1742.70	90.15
	Middle (WT2)	1010.20	1201.00	797.24	69.53
	Shared WT2-WT3	1174.80	1418.00	890.23	82.09
	Downstream (WT3)	408.22	509.22	301.37	22.93
Anchor	Upstream (WT1)	2847.90	3697.90	2166.00	247.42
	Middle (WT2)	837.02	1051.90	625.40	70.49
	Downstream (WT3)	234.83	343.50	134.04	27.08

The first staggered arrangement analysed is modelled with two upstream wind turbines. The surge and pitch motions are displayed in Table 15, and their plots are shown in Figure 11. Due to the system's symmetry, upstream wind turbines show similar surge and pitch motion values. However, the downstream turbine presents a higher mean displacement with the same motion amplitude. The distribution of the dynamic tensions is shown in Table 16, focusing on the maximum tension presented in Figure 12.

Table 15. Surge and pitch motions for a three-spar system in a staggered arrangement with two upstream wind turbines.

Motion	Turbine	Mean	Max	Min	Std
Surge [m]	WT1	67.37	69.84	64.54	0.824
	WT2	67.66	69.97	64.84	0.794
	WT3	73.12	75.40	70.06	0.825
Pitch [deg]	WT1	4.62	5.85	3.10	0.423
	WT2	4.61	6.00	2.91	0.432
	WT3	4.98	6.31	3.29	0.468

Table 16. Dynamic tension for a three-spar system in staggered arrangement with two upstream wind turbines.

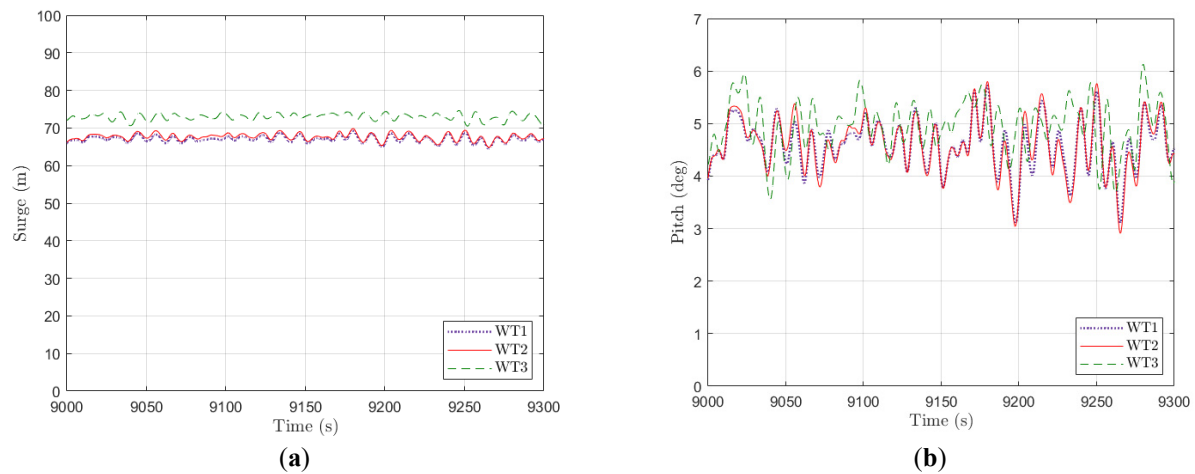| Location	Point	Mean [kN]	Max [kN]	Min [kN]	Std [kN]
Fairlead	Upstream (WT1/WT2)	3021.70	3530.70	2576.20	134.55
	Shared WT1-WT2	2006.30	2113.60	1884.30	30.42
	Shared WT2-WT3	643.22	851.99	429.74	6.44
	Downstream (WT3)	296.06	331.78	263.74	8.20
Anchor	Upstream (WT1/WT2)	2849.30	3362.90	2399.60	135.05
	Downstream (WT3)	122.29	155.74	87.42	9.84

Figure 11. A three-spar system is in a staggered arrangement with two upstream wind turbines: (**a**) surge motion and (**b**) pitch motion.
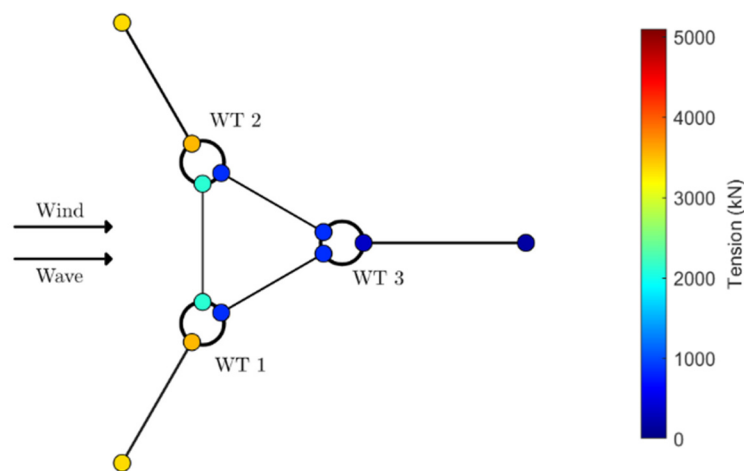

Figure 12. Maximum tension distribution for a three-spar system in a staggered arrangement with two upstream wind turbines.

As with the other systems, the tensions are concentrated on the upstream elements, with a maximum tension of 3530.7 kN on the upstream fairleads. The mean tension values are close to those observed in the tandem configuration with 6 anchors. For comparison, the second staggered model has only one upstream wind turbine and two downstream. The floaters' displacements are detailed in Table 17 and plotted in Figure 13.

Table 17. Surge and pitch motions for a three-spar system in a staggered arrangement with two downstream wind turbines.

Motion	Turbine	Mean	Max	Min	Std
Surge [m]	WT1	31.30	33.75	28.95	0.815
	WT2	66.93	69.59	64.00	0.815
	WT3	66.50	69.06	63.52	0.806
Pitch [deg]	WT1	4.35	5.62	3.02	0.421
	WT2	4.91	6.29	3.27	0.435
	WT3	4.92	6.28	3.24	0.436

(a)   **(b)**
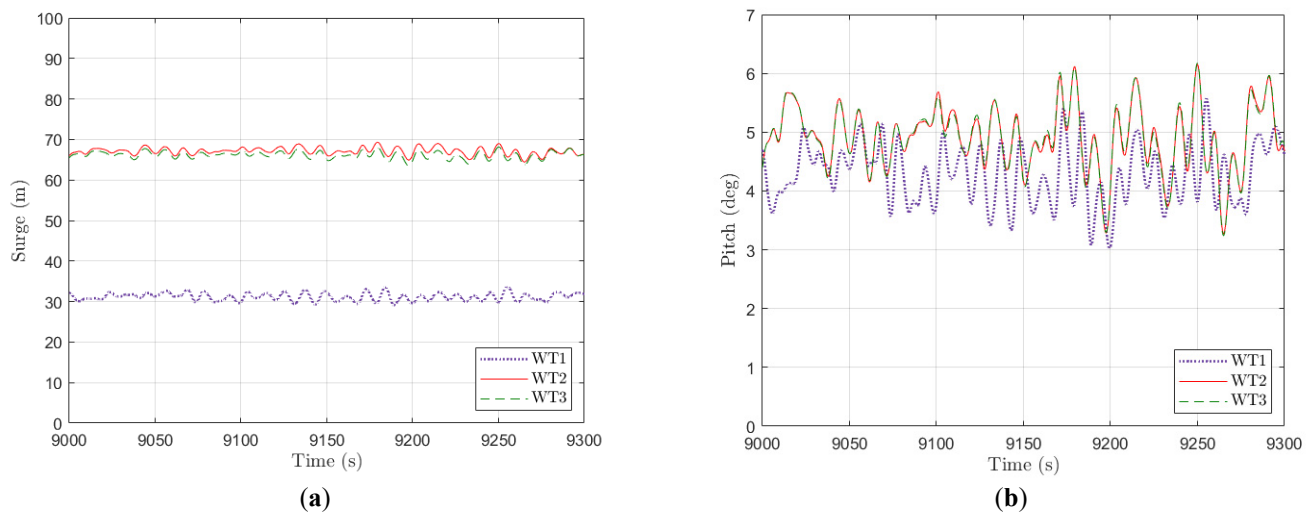
Figure 13. Three-spar system in a staggered arrangement with two downstream wind turbines: (**a**) Surge motion; (**b**) Pitch motion.

The upstream wind turbine has a lower offset value, with a mean surge of 31.3 m. The downstream turbines show a similar behaviour to the two upstream turbines (Table 15) from the previous model. Moreover, the amplitude of motion is shorter for the upstream wind turbine. Due to the restoring forces applied by the upstream anchor line, which are aligned with the environmental loads, the pitch motion for the first platform has a lower inclination than the other two. The dynamic tensions are described in Table 18 for each element of the system. The representation of the maximum global tension can be seen in Figure 14. With only one upstream anchor mooring, the maximum tension at the upstream fairleads is 36.2% higher than that of the other staggered configuration with two upstream turbines. However, the maximum tension at the shared fairleads is lower, meaning less tension is applied to the polyester ropes.

Table 18. Dynamic tension for a three-spar system in a staggered arrangement with two downstream wind turbines.

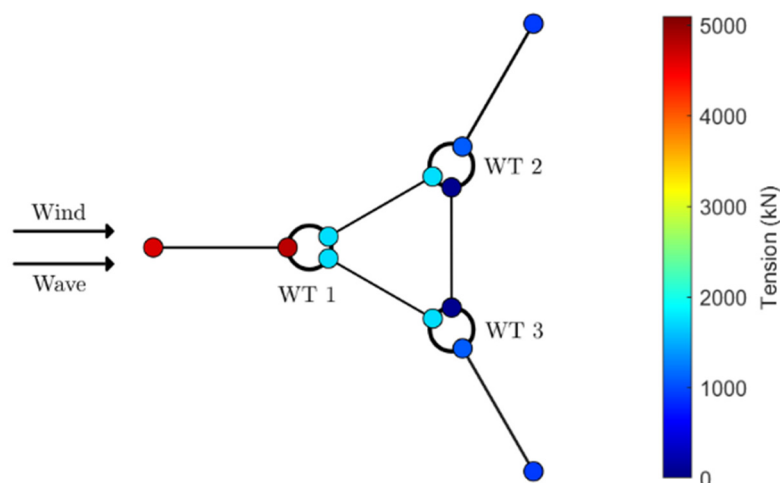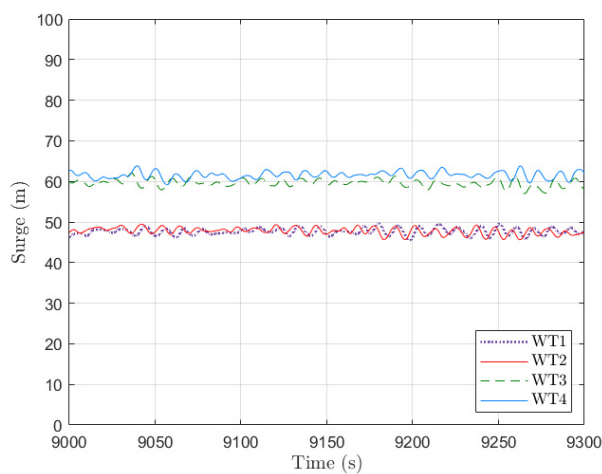| Location	Point	Mean [kN]	Max [kN]	Min [kN]	Std [kN]
Fairlead	Upstream (WT1)	3877.20	4808.50	3076.40	35.03
	Shared WT1-WT2	1458.40	1738.40	1193.20	79.22
	Shared WT2-WT3	32.38	59.58	16.94	6.53
	Downstream (WT2/WT3)	916.41	1082.10	759.84	52.08
Anchor	Upstream (WT1)	3705.50	4640.40	2897.70	352.03
	Downstream (WT2/WT3)	742.21	916.87	591.15	52.74

Figure 14. Maximum tension distribution for a three-spar system in a staggered arrangement with two downstream wind turbines.

Finally, the four-spar systems were modelled and simulated. For the system with perpendicular shared lines, the main motions obtained from the three-hour simulation are displayed in Table 19. Their motion behaviour is shown in

Figure 15. The results reveal the system symmetry, with the two upstream wind turbines showing similar motion values for surge and pitch to the two downstream turbines. The tensions are described in detail in Table 20, and the distribution of the maximum tension is presented in Figure 16. The upstream fairleads and anchor show a high tension, reaching 3797.4 kN in the highest peak response. The shared line between wind turbines 1 and 2 has a higher tension than the other polyester moorings; however, this value represents 42.2% of the material's maximum breaking load.

Table 19. Surge and pitch motions for a four-spar system with 90 degrees.

Motion	Turbine	Mean	Max	Min	Std
Surge [m]	WT1	47.62	50.27	44.98	0.810
	WT2	48.09	51.08	45.39	0.804
	WT3	59.88	62.18	56.88	0.828
	WT4	61.46	64.26	58.73	0.836
Pitch [deg]	WT1	4.54	5.72	3.05	0.411
	WT2	4.52	5.94	2.89	0.423
	WT3	4.96	6.31	3.26	0.483
	WT4	4.96	6.36	3.39	0.441

(a)
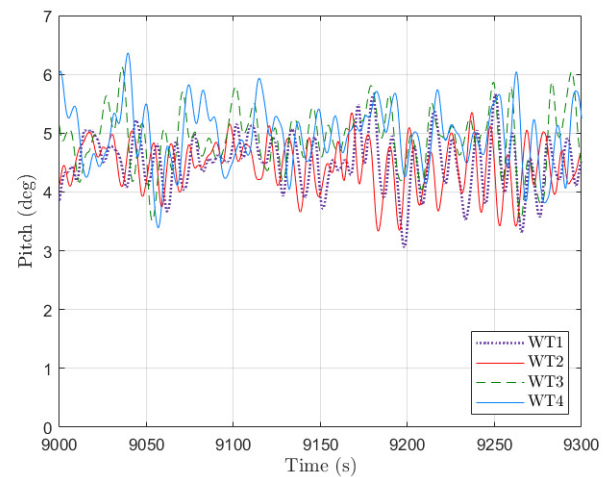
(b)

Figure 15. A four-spar system with 90 degrees: (**a**) Surge motion; (**b**) Pitch motion.

Table 20. Dynamic tension for a four-spar system with 90 degrees.

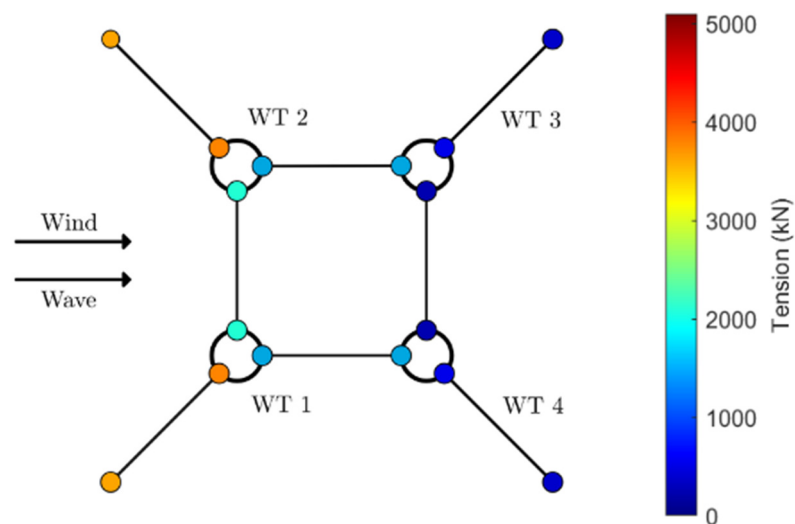| Location	Point	Mean [kN]	Max [kN]	Min [kN]	Std [kN]
Fairlead	Upstream (WT1/WT2)	3171.20	3797.40	2698.90	159.72
	Shared WT1-WT2	1981.90	2070.50	1850.40	286.12
	Shared WT2-WT3	1164.40	1458.00	906.44	78.53
	Shared WT3-WT4	196.37	222.75	173.24	7.34
	Downstream (WT3/WT4)	419.91	514.80	321.83	22.42
Anchor	Upstream (WT1/WT2)	2998.80	3629.90	2521.70	160.80
	Downstream (WT3/WT4)	245.94	358.03	133.90	27.49

Figure 16. Maximum tension distribution for a four-spar system with 90 degrees.

Lastly, the four-spar system with shared lines at 30 degrees about the x-axis is tested. The surge and pitch motion are shown in Table 21 and illustrated in Figure 17. Because of the single upstream line, the first wind turbine behaves like the wind turbine 1 from the staggered system with only one upstream turbine (Table 17). Wind turbines 2 and 3 show matching surge and pitch, since they are symmetric to the environmental loads. The downstream turbine shows a higher motion in both degrees of freedom since low restoring forces come from the anchor lines because they are oriented opposite to the dynamic load's direction. The summarised system tensions are detailed in Table 22, and the maximum column is represented in Figure 18. The upstream elements apply most of the restoring force in the system, presenting the highest values of maximum tension. Moreover, the shared lines show a better tension distribution with lower tension at the fairlead in comparison to the system with perpendicular shared moorings.

Table 21. Surge and pitch motions for a four-spar system with 30 degrees.

Motion	Turbine	Mean	Max	Min	Std
	WT1	32.43	35.16	29.69	0.797
Surge [m]	WT2	56.09	58.64	53.08	0.811
	WT3	55.51	58.61	52.74	0.859
	WT4	67.91	70.41	64.81	0.891
	WT1	4.37	5.62	2.86	0.405
Pitch [deg]	WT2	4.81	6.23	3.38	0.440
	WT3	4.81	6.23	3.31	0.450
	WT4	4.97	6.57	3.42	0.456

Table 22. Dynamic tension for a four-spar system with 90 degrees.

| Location	Point	Mean [kN]	Max [kN]	Min [kN]	Std [kN]
	Upstream (WT1)	4226.00	5048.10	3386.50	309.27
	Shared WT1-WT2	1682.10	1969.90	1447.20	76.69
Fairlead	Middle (WT2/WT3)	1279.50	1621.00	969.40	100.20
	Shared WT2-WT4	640.75	867.74	404.07	66.46
	Downstream (WT4)	311.64	348.43	276.17	7.97
	Upstream (WT1)	4054.60	4883.70	3205.30	311.08
Anchor	Middle (WT2/WT3)	1105.30	1482.70	765.58	106.05
	Downstream (WT4)	137.86	179.25	95.25	10.62
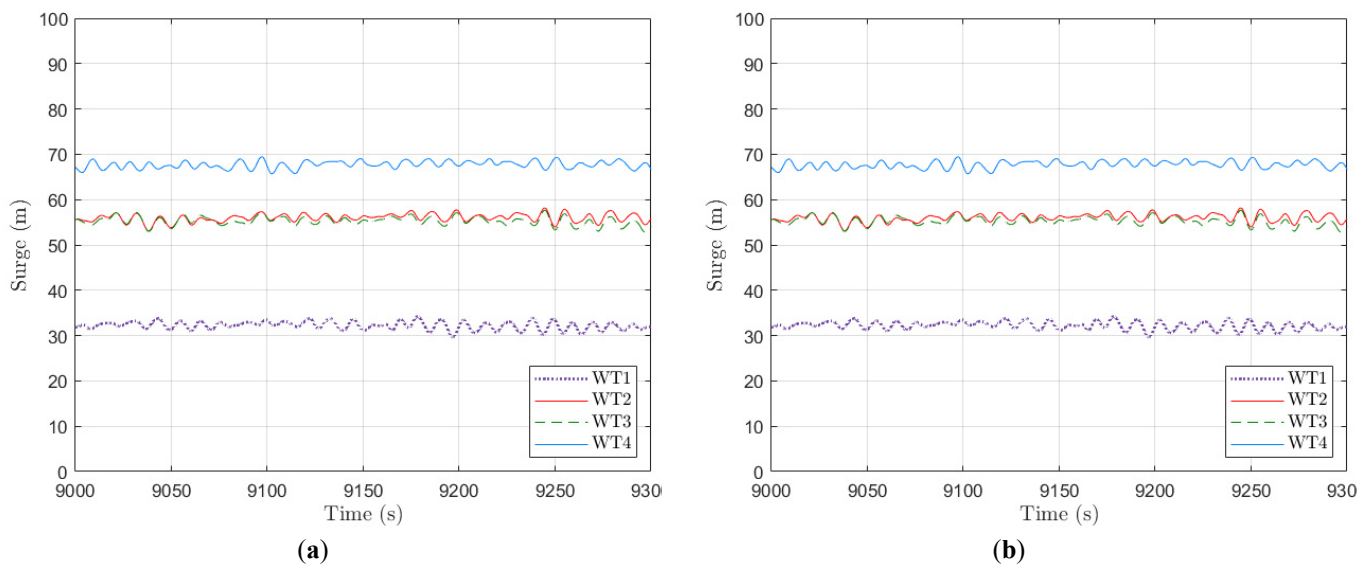
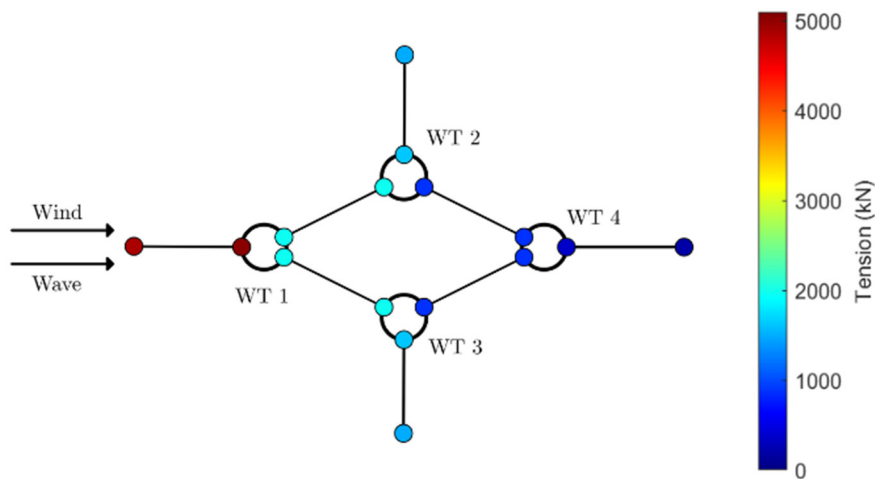**Figure 17.** A four-spar system with 30 degrees: (**a**) Surge motion; (**b**) Pitch motion.

Figure 18. Maximum tension distribution for a four-spar system with 90 degrees.

5. Conclusions

This study focuses on the dynamic analysis of offshore wind farms using shared lines. Different mooring layouts are modelled with SIMA, and their static results are verified using the MoorPy code. The main conclusions obtained from the dynamic response are as follows

- For the tandem arrangement, the motion values for the system with six anchors are more stable since the middle anchor lines apply a restoring force to the second wind turbine. In addition, these elements can likely prevent large sway motions in environmental loads that are not aligned with the *x*-axis. When analysing the mean tensions, there is a better distribution along the system, with less concentrated values on the upstream elements.
- On the staggered model, it is noticeable that the system presenting two upstream turbines has a lower value of maximum tension compared to the system with only one upstream turbine. Nevertheless, the tensions applied to the polyester material are lower for the second system, which may allow a smaller mooring diameter, contributing to savings on the material cost. In relation to the platform motions, the layout with two upstream turbines shows a similar surge displacement for all floaters, with matching amplitude. For the layout with two downstream turbines, the upstream floater showed a smaller value of motion in both surge and pitch degrees of freedom.
- The four-spar systems showed a similar behaviour to the staggered layout. The system with perpendicular shared lines showed closer surge and pitch motion values for all buoys. Meanwhile, the system with 30 degrees showed a first turbine with more stable results due to the restoring upstream anchor line and a less stable motion for the fourth turbine. When the layout uses a single upstream anchor, the system concentrates tension on this line, reducing tension on the shared lines.

- Overall, the staggered layout with two upstream wind turbines and the four-spar system with 90 degrees are the most realistic layouts for wind farm shared subsystems. These models show a more uniform platform's motion response and lower values of maximum tension along the system.

Acknowledgements

Author Contributions

Conceptualization, S.W. and C.G.S.; Methodology, M.V.B., F.J.V., J.D., S.W. and C.G.S.; Software, M.V.B., F.J.V., J.D., S.W. and C.G.S.; Validation, M.V.B., F.J.V., J.D. and S.W.; Formal Analysis, M.V.B., F.J.V. and J.D.; Investigation, M.V.B., F.J.V., J.D.; Resources, S.W. and C.G.S.; Data Curation, M.V.B., F.J.V., J.D., S.W. and C.G.S.; Writing—Original Draft Preparation, M.V.B., F.J.V., J.D. and S.W.; Writing—Review & Editing, M.V.B., F.J.V., J.D., S.W. and C.G.S.; Visualization, M.V.B., F.J.V. and J.D.; Supervision, S.W. and C.G.S.; Project Administration, C.G.S.; Funding Acquisition, C.G.S.

Ethics Statement

Not applicable.

Informed Consent Statement

Not applicable.

Data Availability Statement

Access to the data examined in this study can be obtained by contacting the corresponding author.

Funding

Declaration of Competing Interest

The authors declare that they have no known competing financial interests or personal relationships that could have appeared to influence the work reported in this paper.

References

1. Esteban MD, Diez JJ, López JS, Negro V. Why offshore wind energy? *Renew Energy* **2011**, *36*, 444–450.
2. Diaz HM, Guedes Soares C. Review of the current status, technology and future trends of offshore wind farms. *Ocean Eng.* **2020**, *209*, 107381.
3. Anaya-Lara O, Tande JO, Uhlen K, Merz K. *Offshore Wind Energy Technology*; John Wiley & Sons: Hoboken, NJ, USA, 2018; pp. 1–320.
4. Li J, Yu XB. Onshore and offshore wind energy potential assessment near Lake Erie shoreline: A spatial and temporal analysis. *Energy* **2018**, *147*, 1092–1107.
5. Diaz HM, Guedes Soares C. Cost and financial evaluation model for the design of floating offshore wind farms. *Ocean Eng.* **2023**, *287*, 115841.
6. Kang JC, Guedes Soares C. An opportunistic maintenance policy for the offshore wind farms. *Ocean Eng.* **2020**, *216*, 108075.
7. Guedes Soares C, Bento AR, Goncalves M, Silva D, Martinho P. Numerical evaluation of the wave energy resource along the Atlantic European coast. *Comput. Geosci.* **2014**, *71*, 37–49.
8. Diaz HM, Serna J, Nieto J, Guedes Soares C. Market needs, opportunities and barriers for the floating wind industry. *J. Mar. Sci. Eng.* **2022**, *10*, 934.
9. Montes A, Fournely D, Sørensen JN, Larsen GC. Techno-Economic Modeling of Floating Wind Farms. *Energies* **2025**, *18*, 967. doi:10.3390/en18040967.
10. Chen J, Hu Z, Liu G, Wan D. Coupled aero-hydro-servo-elastic methods for floating wind turbines. *Renew Energy* **2019**, *130*, 139–153.

11. Ramos-García N, Sessarego M, Horcas SG. Aero-hydro-servo-elastic coupling of a multi-body finite-element solver and a multi-fidelity vortex method. *Wind Energy* **2021**, *24*, 481–501.

12. Dou S, Pegalajar-Jurado A, Wang S, Bredmose H, Stolpe M. Optimization of floating wind turbine support structures using frequency-domain analysis and analytical gradients. *J. Phys. Conf. Ser.* **2020**, *1618*, 042028.

13. Ma KT, Luo Y, Kwan CTT, Wu Y. *Mooring System Engineering for Offshore Structures*; Gulf Professional Publishing: Houston, TX, USA, 2019; pp. 1–512.

14. Zhang W, Calderon-Sanchez J, Duque D, Souto-Iglesias A. Computational fluid dynamics (CFD) applications in floating offshore wind turbine (FOWT) dynamics: A review. *Appl. Ocean Res.* **2024**, *150*, 104075.

15. Otter A, Murphy J, Pakrashi V, Robertson A, Desmond C. A review of modelling techniques for floating offshore wind turbines. *Wind Energy* **2022**, *25*, 831–857.

16. Thomsen JB, Bergua R, Jonkman J, Robertson A, Mendoza N, Brown C, et al. Modeling the TetraSpar floating offshore wind turbine foundation as a flexible structure in OrcaFlex and OpenFAST. *Energies* **2021**, *14*, 7866.

17. Chen H, Hall M. CFD simulation of floating body motion with mooring dynamics: Coupling MoorDyn with OpenFOAM. *Appl. Ocean Res.* **2022**, *124*, 103210.

18. Robertson AN, Wendt F, Jonkman JM, Popko W, Dagher H, Gueydon S, et al. OC5 Project Phase II: Validation of global loads of the DeepCwind floating semisubmersible wind turbine. *Energy Procedia.* **2017**, *137*, 38–57.

19. Uzunoglu E, Guedes Soares C. On the model uncertainty of wave induced platform motions and mooring loads of a semisubmersible based wind turbine. *Ocean Eng.* **2018**, *148*, 277–285.

20. Duan F, Hu Z, Niedzwecki JM. Model test investigation of a spar floating wind turbine. *Mar. Struct.* **2016**, *49*, 76–96.

21. Ahn HJ, Shin H. Model test and numerical simulation of OC3 spar type floating offshore wind turbine. *Int. J. Nav. Archit. Ocean Eng.* **2019**, *11*, 1–10.

22. Xu X, Day S. Experimental investigation on dynamic responses of a spar-type offshore floating wind turbine and its mooring system behaviour. *Ocean Eng.* **2021**, *236*, 109488.

23. Hsu WT, Thiagarajan KP, Manuel L. Extreme mooring tensions due to snap loads on a floating offshore wind turbine system. *Mar. Struct.* **2017**, *55*, 182–199.

24. Kvitrud A. Lessons learned from Norwegian anchor line failures 2010–2013. In Proceedings of the 33rd International Conference on Ocean, Offshore and Arctic Engineering, San Francisco, CA, USA, 8–13 June 2014.

25. Xu S, Wang S, Guedes Soares C. Review of mooring design for floating wave energy converters. *Renew. Sustain. Energy Rev.* **2019**, *111*, 595–621.

26. Xu S, Wang S, Guedes Soares C. Experimental study of the influence of the rope material on mooring fatigue damage and point absorber response. *Ocean Eng.* **2021**, *232*, 108667.

27. Lin TH, Yang RY. Stability analysis and environmental influence evaluation on a hybrid mooring system for a floating offshore wind turbine. *J. Mar. Sci. Eng.* **2023**, *11*, 2236.

28. Lian Y, Zhong F, Zheng J, Chen W, Ma G, Wang S, et al. Effects of mooring line with different materials on the dynamic response of offshore floating wind turbine. *J. Mar. Sci. Eng.* **2023**, *11*, 2302.

29. Xu S, Wang S, Liu H, Zhang Y, Li L, Guedes Soares C. Experimental evaluation of the dynamic stiffness of synthetic fibre mooring ropes. *Appl. Ocean Res.* **2021**, *112*, 102709.

30. Lian Y, Liu H, Zhang Y, Li L. An experimental investigation on fatigue behaviors of HMPE ropes. *Ocean Eng.* **2017**, *139*, 237–249.

31. Feng L, Wang Q, Wang S, Xu S. Experimental characterization of stiffness of a polyester mooring rope for a CFPSO. *J. Mar. Sci. Eng.* **2024**, *12*, 1435.

32. Pham HD, Cartraud P, Schoefs F, Soulard T, Berhault C. Dynamic modelling of nylon mooring lines for a floating wind turbine. *Appl. Ocean Res.* **2019**, *87*, 1–8.

33. Depalo F, Wang S, Xu S, Soares CG, Yang SH, Ringsberg JW. Effects of dynamic axial stiffness of elastic moorings for a wave energy converter. *Ocean Eng.* **2022**, *251*, 111132.

34. Liang G, Jiang Z, Merz K. Dynamic analysis of a dual-spar floating offshore wind farm with shared moorings in extreme environmental conditions. *Mar. Struct.* **2023**, *90*, 103441.

35. Goldschmidt M, Muskulus M. Coupled mooring systems for floating wind farms. *Energy Procedia* **2015**, *80*, 255–262.

36. Lopez-Olocco T, Liang G, Medina-Manuel A, Ynocente LS, Jiang Z, Souto-Iglesias A. Experimental comparison of a dual-spar floating wind farm with shared mooring against a single floating wind turbine under wave conditions. *Eng. Struct.* **2023**, *292*, 116475.

37. Hall M, Lozon E, Housner S, Sirnivas S. Design and analysis of a ten-turbine floating wind farm with shared mooring lines. *J. Phys. Conf. Ser.* **2022**, *2362*, 012016.

38. Falkenberg E, Ahjem V, Yang L. Best practice for analysis of polyester rope mooring systems. In *Proceedings of the Offshore Technology Conference*; OTC: Houston, TX, USA, 2017; p. D031S034R006. doi:10.4043/27761-MS.

39. SINTEF Ocean. *SIMA 4.8.0 Documentation*; SINTEF Ocean: Trondheim, Norway, 2024.

40. Vidal FJ, Wang S, Guedes Soares C. Dynamic modelling of synthetic moorings for a wave energy converter. In *Innovations in Renewable Energies Offshore*; CRC Press: Boca Raton, FL, USA, 2024; pp. 437–445. doi:10.1201/9781003558859-48.

41. Guedes Soares C. Representation of double-peaked sea wave spectra. *Ocean Eng.* **1984**, *11*, 185–207.

42. Jonkman J. *Definition of the Floating System for Phase IV of OC3. NREL/TP-500-47535*; National Renewable Energy Lab (NREL): Golden, CO, USA, 2010.

43. Jonkman J, Butterfield S, Musial W, Scott G. *Definition of a 5-MW Reference Wind Turbine for Offshore System Development. NREL/TP-500-38060*; National Renewable Energy Lab (NREL): Golden, CO, USA, 2009.

44. Fu C, Zhang Z, Yu M, Zhou D, Zhu H, Duan L, et al. Research on Aerodynamic Characteristics of Three Offshore Wind Turbines Based on Large Eddy Simulation and Actuator Line Model. *J. Mar. Sci. Eng.* **2024**, *12*, 1341.

45. Cottura L, Caradonna R, Novo R, Ghigo A, Bracco G, Mattiazzo G. Effect of pitching motion on production in a OFWT. *J. Ocean Eng. Mar Energy* **2022**, *8*, 319–330.

46. Bridon. Fibre Rope Catalogue. Available online: https://www.yumpu.com/en/document/read/33598438/fibre-rope-catalogue-bridon (accessed on 21 March 2025).

47. Biroli MV, Wang S, Guedes Soares C. Dynamic analysis comparison of shared mooring system for offshore wind turbine platforms. In *Innovations in Renewable Energies Offshore*; CRC Press: Boca Raton, FL, USA, 2024; pp. 369–378. doi:10.1201/9781003558859-41.

48. Balakrishnan K, Arwade SR, DeGroot DJ, Fontana C, Landon M, Aubeny CP. Comparison of multiline anchors for offshore wind turbines with spar and with semisubmersible. *In. J. Phys. Conf. Ser.* **2020**, *1452*, 012032.

49. Hall M, Housner S, Sirnivas S, Wilson S. *MoorPy (Quasi-Static Mooring Analysis in Python)*; USDOE Office of Energy Efficiency and Renewable Energy: Washington, DC, USA, 2021. doi:10.11578/dc.20210726.1.